Nanoscale Res Lett (2010) 5:701–708
DOI 10.1007/s11671-010-9534-0

NANO EXPRESS

Functionalized Mesoporous SBA-15 with CeF_3: Eu^{3+} Nanoparticle by Three Different Methods: Synthesis, Characterization, and Photoluminescence

Ying Li · Bing Yan

Received: 1 December 2009 / Accepted: 5 January 2010 / Published online: 16 January 2010

Abstract Luminescence functionalization of the ordered mesoporous SBA-15 silica is realized by depositing a CeF_3: Eu^{3+} phosphor layer on its surface (denoted as CeF_3: Eu^{3+}/SBA-15/IS, CeF_3: Eu^{3+}/SBA-15/SI and CeF_3: Eu^{3+}/SBA-15/SS) using three different methods, which are reaction in situ (I-S), solution impregnation (S-I) and solid phase grinding synthesis (S-S), respectively. The structure, morphology, porosity, and optical properties of the materials are well characterized by X-ray diffraction, Fourier transform infrared spectroscopy, transmission electron microscopy, N_2 adsorption, and photoluminescence spectra. These materials all have high surface area, uniformity in the mesostructure and crystallinity. As expected, the pore volume, surface area, and pore size of SBA-15 decrease in sequence after deposition of the CeF_3: Eu^{3+} nanophosphors. Furthermore, the efficient energy transfer in mesoporous material mainly occurs between the Ce^{3+} and the central Eu^{3+} ion. They show the characteristic emission of Ce^{3+} 5d → 4f (200–320 nm) and Eu^{3+} $^5D_0 \rightarrow {}^7F_J$ ($J = 1$–4, with $^5D_0 \rightarrow {}^7F_1$ orange emission at 588 nm as the strongest one) transitions, respectively. In addition, for comparison, the mesoporous material CeF_3: Eu^{3+}/SBA-15/SS exhibits the characteristic emission of Eu^{3+} ion under UV irradiation with higher luminescence intensity than the other materials.

Keywords Mesoporous material · Nanoparticle · Luminescence · Cerium trifluoride doped with europium ion

Y. Li · B. Yan (✉)
Department of Chemistry, Tongji University, 200092 Shanghai, China
e-mail: byan@tongji.edu.cn

Introduction

In the past decades, inorganic luminescent materials with nanosale dimensions have been found many potential applications, such as light emitting devices, low-threshold lasers, optical amplifiers, biological fluorescence labeling, and so on [1–4]. However, due to nonradiative decay from defects on the surface of the nanocrystals, the luminescence efficiency of nanostructural materials is usually lower than that of the corresponding bulk materials [5, 6]. To reduce these defects, the growth of a crystalline shell of a suitable inorganic material around each nanocrystal to form the core/shell structures has been regarded as an effective strategy to improve luminescent efficiency. Compared with the conventional oxide-based luminescent materials, fluorides are advantageous as fluorescent host materials owing to their low vibrational energies, and the subsequent minimization of the quenching of the excited state of the rare-earth ions [7]. Hence, Lanthanide fluorides have attracted considerable attention because of their outstanding luminescent characteristics that originate from good coordination capability of hosted lanthanide ions in fluoride lattices and the wide band gap and very low vibrational energies induced by the high ionicity of the lanthanide to fluoride bond [8–13]. A bulk crystal of CeF_3 possesses a hexagonal phase structure with a space group of *P*63/*mcm* (JSPDS 08-0045) and lattice constants $a = 0.713$ nm, $c = 0.729$ nm, and there are six formula weights per unit cell. The Ce^{3+} ion in the CeF_3 crystal is coordinated by nine F^- and has a *C*2 site symmetry [9]. As a potential scintillator and tunable laser material, CeF_3 is a luminescent material with 100% activator concentration. Moreover, the material CeF_3: Eu^{3+} has red luminescence property, the energy transfer processes from

Ce^{3+} to Eu^{3+} can enhance the Eu^{3+} emission, which has gained a great deal of research interest.

Mesoporous materials with unique properties, such as high surface area, controlled pore structure and uniform pore size distribution, are of great interest for adsorption, sensing, catalysis, and other applications [14–19]. Among them, SBA-15 is by far the largest pore size mesochannels, with thick walls, adjustable pore size from 3 to 30 nm, and high hydrothermal and thermal stability. Since the discovery of triblock copolymer-templated SBA-15 in 1998 [20], the adsorption and surface properties of this mesoporous material have been adjusted by anchoring a variety of functional groups onto the surface. Recently, ordered mesoporous SBA-15 has gained considerable attention as an ideal host for incorporation of active molecules because of their stable mesoporous structure, tunable pore size, and high specific surface area within abundant Si–OH active bonds on the pore walls, nontoxic nature, well-defined surface properties, and good biocompatibility [21–26]. In addition, surface-functionalized mesoporous silica materials can be used as excellent hosts for a variety of guest molecules. Luminescence functionalization of inorganic porous materials (using YVO_4: Eu^{3+}, rare-earth complex, etc.) has been reported in several publications [27–29]. It is shown that the promising visible luminescent properties can be obtained by linking the rare-earth complexes to the mesoporous materials.

Herein, we propose a novel design on the synthesis and characterization of the mesoporous luminescence material by incorporating CeF_3: Eu^{3+} nanophosphors into the surface of mesoporous SBA-15 using three different methods: reaction in situ (I-S), solution impregnation(S-I), and solid phase grinding synthesis (S-S), respectively. The obtained composite materials were well characterized by SAXRD (Small Angle X-rays Diffraction), FTIR (Fourier Transform Infrared Spectroscopy), N_2 adsorption/desorption analysis, TEM (Transmission Electron Microscopy), HRTEM (High-Resolution Transmission Electron Microscopy), and luminescence spectra. Comparative studies on the luminescence properties of all these synthesized materials were investigated in relation to guest–host interactions between the guest molecule and the silica matrix.

Experimental Section

Materials

Pluronic P123 ($EO_{20}PO_{70}EO_{20}$, Aldrich), tetraethoxysilane (TEOS, Aldrich). Europium nitrate was prepared by dissolving Eu_2O_3 in concentrated nitric acid.

Synthetic Procedures

Method I: Solution Impregnation (S-I) Synthesis of Mesoporous SBA-15 and Functionalized Mesoporous SBA-15 by CeF_3: Eu (Denoted as CeF_3: Eu^{3+}/SBA-15/SI)

SBA-15 was synthesized according to the procedure as follows: 1.0 g P123 was dissolved in 7.5 g of H_2O and 30.0 g of dilute HCl solution (2.0 M) with stirring at 35°C. Then, 2.125 g of TEOS was added dropwise to the solution with stirring, and the mixed solution (15 mL) was transferred into a Teflon bottle sealed in an autoclave (2 MPa, 25 mL), which was heated at 100°C for 48 h. The obtained material was filtered, washed, and dried in air at room temperature. The as-synthesized material was calcined from room temperature to 550°C at a heating rate of 1°C min^{-1} and kept at 550°C for 6 h to remove the templates.

Deposition of the CeF_3: Eu^{3+} phosphor layer onto the surface of the template-free SBA-15 was prepared using solution impregnation (S-I) by a sol–gel process [9]. The doping concentration of Eu^{3+} was 5 mol % of Ce^{3+} in CeF_3. In a typical process, 1.9 mmol Ce $(NO_3)_3{\cdot}6H_2O$ and 0.1 mmol of $Eu(NO_3)_3{\cdot}6H_2O$ were dissolved in 12 mL *N*,*N*-dimethyl-formamide (DMF), and then a solution of diethylene glycol (DEG 25 mL) containing 6 mmol of NH_4F was injected into the DMF solution. The mixture was stirred at 200°C for 1 h to form a stable sol. Then desired amount of the template-free SBA-15 powder was added into the sol with stirring. The suspension was stirred for another 3 h, and then the resulting material was separated by centrifugation, washed several times with distilled water and absolute ethanol, and finally dried at 60°C.

Method II: Reaction In situ (I-S) (Denoted as CeF_3: Eu^{3+}/SBA-15/IS)

In this process, 1.0 g P123 was dissolved in 7.5 g of H_2O and 30.0 g of dilute HCl solution (2.0 M) with stirring at 35°C (Solution 1). At the same time, 1.9 mmol $Ce(NO_3)_3{\cdot}6H_2O$ and 0.1 mmol of $Eu(NO_3)_3{\cdot}6H_2O$ were dissolved in 12 mL *N*,*N*-dimethyl- formamide (DMF), and then a solution of diethylene glycol (DEG 25 mL) containing 6 mmol of NH_4F was injected into the DMF solution. The mixture was stirred for 1 h to form a stable sol (solution 2). Then, 2.125 g of TEOS was added dropwise to the solution 2 with stirring, and the mixed solution was soaked in about 25 mL of Solution 1. After stirring 1 h at the room temperature, the mixture was transferred into a Teflon bottle sealed in an autoclave (2 MPa, 25 mL), which was heated at 120°C for 48 h. The obtained material was filtered, washed, and dried in

air at room temperature. The as-synthesized material was calcined from room temperature to 550°C at a heating rate of 1°C min^{-1} and kept at 550°C for 6 h to remove the templates.

Method III: Solid Phase Grinding Synthesis (S-S) (Denoted as CeF_3: Eu^{3+}/SBA-15/SS)

CeF_3: Eu^{3+}solid precipitate was prepared in a typical procedure as follows: 1.9 mmol Ce $(NO_3)_3{\cdot}6H_2O$ and 0.1 mmol of $Eu(NO_3)_3{\cdot}6H_2O$ were dissolved in 25 mL of diethylene glycol (DEG, 98.0%) in a round-bottomed flask at 100°C under stirring to form a clear solution. The solution was then heated in a silicon oil bath under vigorous stirring with a flow of N_2 atmosphere, and the temperature of the solution was further increased to 200°C. At this temperature, a solution of DEG (25 mL) containing 6 mmol of NH_4F was injected into the solution, and the mixture was kept at 200°C for 1 h. Then, the obtained suspension was cooled to room temperature and diluted with 50 mL of ethanol. The solid particles were separated by centrifugation.

A typical procedure for the preparation of pure mesoporous SBA-15 powder was synthesized according to the literature by using a triblock copolymer as the template [20]. The result material CeF_3: Eu^{3+}/SBA-15/SS was obtained by the mixture of CeF_3: Eu^{3+} solid precipitate and SBA-15 powder using solid phase grinding at the room temperature for 2 h and dried at 60°C.

Physical Characterization

X-ray powder diffraction patterns were recorded on a Rigaku D/max-rB diffractometer equipped with a Cu anode in a 2θ range from 0.6° to 6°. IR spectra were measured within the 4,000–400 cm^{-1} region on an infrared spectrophotometer with the KBr pellet technique. Nitrogen adsorption/desorption isotherms were measured at the liquid nitrogen temperature, using a Nova 1000 analyzer. Surface areas were calculated by the Brunauer–Emmett–Teller (BET) method, and pore size distributions were evaluated from the desorption branches of the nitrogen isotherms using the Barrett–Joyner–Halenda (BJH) model. The fluorescence excitation and emission spectra were obtained on a RF-5301 spectrophotometer. Luminescence lifetime measurements were carried out on an Edinburgh FLS920 phosphorimeter using a 450 w xenon lamp as excitation source. Transmission electron microscope (TEM) experiments were conducted on a JEOL2011 microscope operated at 200 kV or on a JEM-4000EX microscope operated at 400 kV.

Results and Discussion

FTIR (Fourier Transform Infrared Spectroscopy)

The presence of the CeF_3: Eu^{3+} nanoparticles functionalized mesoporous SBA-15 by three different methods are characterized by FT-IR spectra. The IR spectra are compared for CeF_3: Eu^{3+} (a), SBA-15 (b), CeF_3: Eu^{3+}/SBA-15/SI (c), CeF_3: Eu^{3+}/SBA-15/IS (d), and CeF_3: Eu^{3+}/SBA-15/SS (e), respectively, and the main absorption and their assignment are shown in Fig. 1. In the case of the SBA-15 host material (b), the obvious absorption bands are present from –OH– (3,450 cm^{-1}), Si–O–Si (ν_{as}, 1,082 cm^{-1}; ν_s, 805 cm^{-1}), Si–OH (ν_s, 962 cm^{-1}), Si–O (δ, 461 cm^{-1}), and H_2O (1,630 cm^{-1}) [30, 31]. Compared with SBA-15, the functionalized mesoporous materials exhibit not only the similar infrared absorption bands as the silica framework but also the peaks at around 1,589 and 1,385 cm^{-1}, which just is originated from the CeF_3: Eu^{3+}, suggesting the formation of crystalline phase (CeF_3: Eu^{3+}) on the surface of mesoporous silica during the heat treatment process.

Power SAXRD (Small Angle X-rays Diffraction) and WAXRD (Wide Angle X-rays Diffraction)

Figure 2 shows the small angle XRD patterns of pure SBA-15, CeF_3: Eu^{3+}/SBA-15/SI, CeF_3: Eu^{3+}/SBA-15/IS, and CeF_3: Eu^{3+}/SBA-15/SS. All the samples exhibit three well-resolved diffraction peaks that can be indexed as (100), (110), and (200) reflections associated with 2-Dhexagonal symmetry (*P6 mm*), confirming a well-ordered mesoporous structure in these material systems. The results indicate that the ordered hexagonal mesoporous structure of SBA-15 remains intact after the deposition of

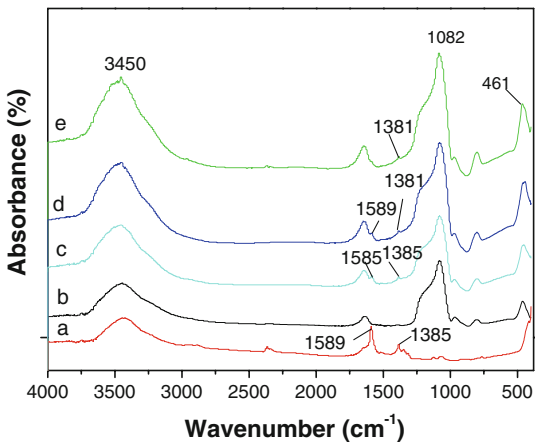

Fig. 1 IR spectra for CeF_3: Eu^{3+} (**a**), SBA-15 (**b**), CeF_3: Eu^{3+}/SBA-15/SI (**c**), CeF_3: Eu^{3+}/SBA-15/SS (**d**) and CeF_3: Eu^{3+}/SBA-15/IS (**e**)

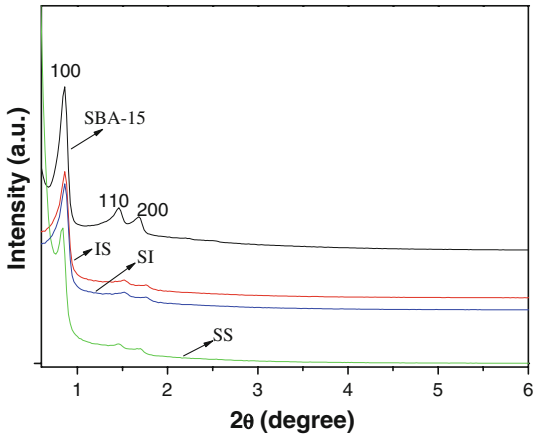

Fig. 2 SAXRD patterns of SBA-15, CeF_3: Eu^{3+}/SBA-15/SI, CeF_3: Eu^{3+}/SBA-15/SS and CeF_3: Eu^{3+}/SBA-15/IS

the CeF_3: Eu^{3+} phosphor layer. However, the intensity of these characteristic diffraction peaks decreases slightly after deposition of CeF_3: Eu^{3+}. This may be caused by the deposition of CeF_3: Eu^{3+} onto the mesoporous framework of SBA-15, which results in the decrease in crystallinity of the mesoporous materials [27].

Figure 3 displays the wide-angle XRD patterns of the corresponding samples. In Fig. 3a for SBA-15, the broad band centered at $2\theta = 22°$ can be assigned to the characteristic reflection from amorphous SiO_2 (JCPDS 29-0085) [11]. While for CeF_3: Eu^{3+}/SBA-15/IS (Fig. 3b), the typical characteristic diffraction peaks of CeF_3 (JCPDS No. 08-0045) can be observed [32], suggesting the successful crystallization of CeF_3: Eu^{3+} on the surface of mesoporous SBA-15.

N_2 Adsorption/Desorption

N_2 adsorption–desorption isotherms are used as a macroscopic average measurement for exploring surface area,

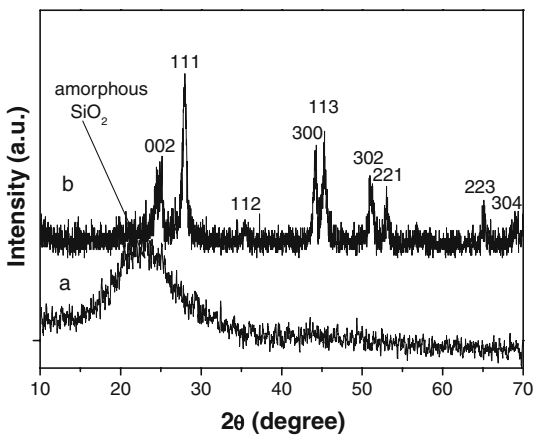

Fig. 3 WAXRD patterns of SBA-15 (**a**), CeF_3: Eu^{3+}/SBA-15/IS (**b**)

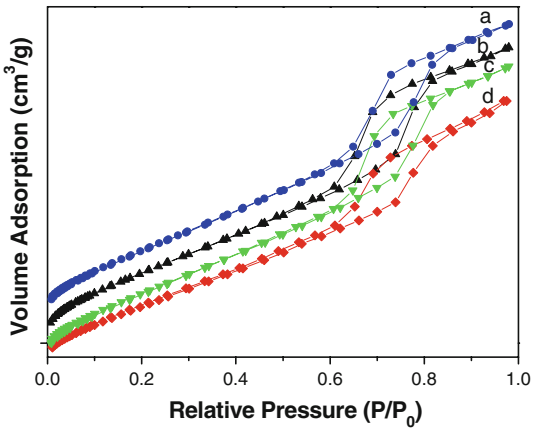

Fig. 4 N_2 adsorption/desorption isotherms of pure SBA-15 (**a**), CeF_3: Eu^{3+}/SBA-15/SI (**b**), CeF_3: Eu^{3+}/SBA-15/SS (**c**) and CeF_3: Eu^{3+}/SBA-15/IS (**d**)

pore diameter, and pore volume of the material. The N_2 adsorption–desorption isotherm and pore size distribution for CeF_3: Eu^{3+}/SBA-15/SI, CeF_3: Eu^{3+}/SBA-15/IS, CeF_3: Eu^{3+}/SBA-15/SS, and pure SBA-15 samples are shown in Fig. 4. They all display Type IV isotherms with H1-type hysteresis loops at high relative pressure according to the IUPAC classification [33–35], characteristic of mesoporous materials with highly uniform size distributions. From the two branches of adsorption–desorption isotherms, the presence of a sharp adsorption step in the P/P_0 region from 0.6 to 0.8 and a hysteresis loop at the relative pressure $P/P_0 > 0.7$ shows that the materials possess a well-defined array of regular mesopores. The specific area and the pore size have been calculated by using Brunauer–Emmett–Teller (BET) and Barrett–Joyner–Halenda (BJH) methods, respectively. The structure data of all these mesoporous materials (BET surface area, total pore volume, and pore size, etc.) are summarized in Table 1. The calcined SBA-15 has a high BET surface area (1,196 m^2/g), a large pore volume (1.81 cm^3/g), and pore size (7.39 nm), indicative of its potential application as a host in luminescence materials. After functionalized with CeF_3: Eu^{3+}, the result material exhibits a smaller specific area and a slightly smaller pore size and pore volume in comparison with

Table 1 Textural data of SBA-15, CeF_3: Eu^{3+}/SBA-15/SI, CeF_3: Eu^{3+}/SBA-15/SS and CeF_3: Eu^{3+}/SBA-15/IS

Sample	d (100)	S_{BET} (m^2/g)	V (cm^3/g)	D_{BJH} (nm)	a_0
SBA-15	10.76	1,196	1.81	7.39	12.42
CeF_3: Eu^{3+}/SBA-15/SI	10.32	975	1.62	6.46	11.91
CeF_3: Eu^{3+}/SBA-15/SS	10.30	996	1.63	6.46	11.88
CeF_3: Eu^{3+}/SBA-15/IS	10.57	874	1.46	6.47	12.20

d_{100} d(100) spacing, a_0 the cell parameter($a_0 = 2d_{100}/\sqrt{3}$), S_{BET} the BET surface area, V the pore volume, D the pore diameter

those of pure SBA-15, which may be due to the presence of nano phosphors CeF_3: Eu^{3+} on the pore surface. Furthermore, it can be deduced that the deposition of CeF_3: Eu^{3+} has not greatly changed the pore structure of mesoporous SBA-15, which coincides with the XRD results.

High-Resolution Transmission Electron Microscopy (HRTEM)

From the HRTEM images (as shown in Fig. 5) of CeF_3: Eu^{3+}/SBA-15/IS, it can be found that the ordered pore structure was still substantially conserved after the deposition of CeF_3: Eu^{3+}. It confirms that the suggested *p6mm* symmetry and a well-ordered hexagonal structure, which is also in agreement with the SAXRD and N_2 adsorption/desorption isotherms. The distance between the centers of the mesopore is estimated to be 10.32 nm, taking good agreement with the value determined from the corresponding XRD data (see Table 1).

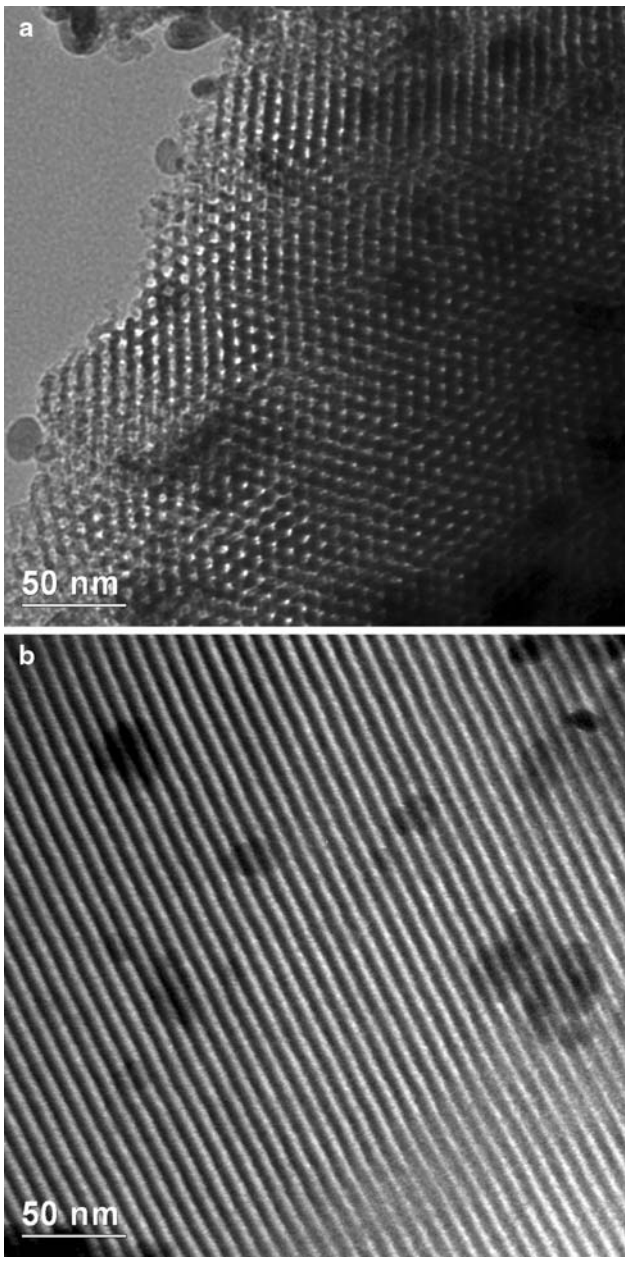

Fig. 5 HRTEM images of CeF_3: Eu^{3+}/SBA-15/IS recorded along the [110] (**a**) and [100] (**b**) zone axes

Photoluminescence Properties

Luminescence measurements have been carried on CeF_3: Eu^{3+} nanoparticles and all the mesoporous materials at room temperature. Figure 6 shows the normalized excitation and emission spectra for CeF_3: Eu^{3+}/SBA-15/SI, CeF_3: Eu^{3+}/SBA-15/IS, and CeF_3: Eu^{3+}/SBA-15/SS. The excitation spectra of these materials were all obtained by monitoring the strongest emission wavelength of the Eu^{3+} ions at 588 nm. As shown in Fig. 6a, the excitation band becomes narrower, and the maximum excitation wavelength shifts from 395 to 341 nm for CeF_3: Eu^{3+}/SBA-15/IS (See Fig. 6 IS). The blue shift of the excitation bands

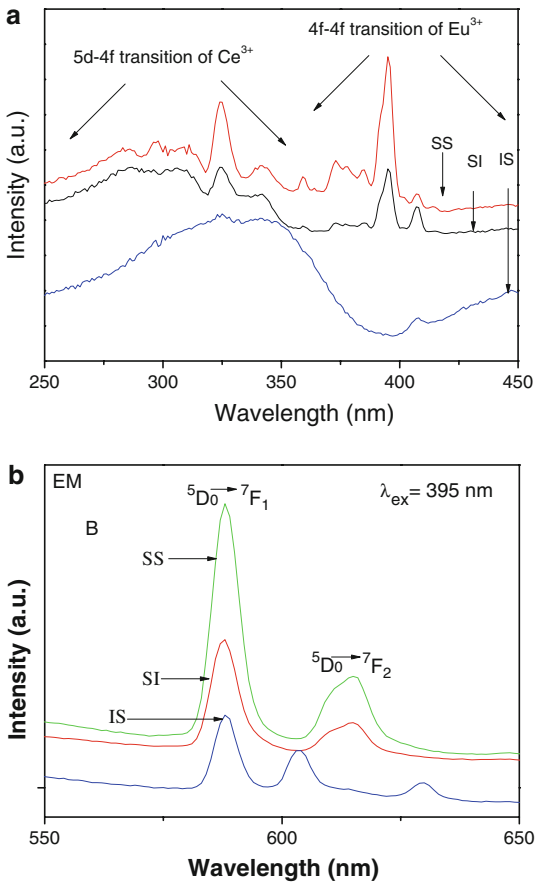

Fig. 6 The excitation (**a**) and emission (**b**) spectra for CeF_3: Eu^{3+}/SBA-15/SI, CeF_3: Eu^{3+}/SBA-15/SS, and CeF_3: Eu^{3+}/SBA-15/IS

can be observed as the introduction of CeF_3: Eu^{3+} into the mesoporous material SBA-15. In the case of CeF_3: Eu^{3+}/SBA-15/SI (as shown in Fig. 6 SI) and CeF_3: Eu^{3+}/SBA-15/SS (Fig. 6 SS), the maximum absorptions of their excitation spectra are similar to the pure CeF_3: Eu^{3+} nanoplates at 395 nm resulting from $f \rightarrow f$ transition of Eu^{3+}.

From the emission spectra of all the materials in Fig. 6b, characteristic Eu^{3+} ion emissions are observed. It can be clearly seen that mainly bands in the 450–700 nm range, which are assigned to the $^5D_0 \rightarrow {}^7F_J$ ($J = 1$–4) transitions at 588, 615, 650 and 700 nm, respectively. The orange–red emission lines at around 588 nm originating from the magnetic dipole transition $^5D_0 \rightarrow {}^7F_1$ are the dominant bands for the materials. The $^5D_0 \rightarrow {}^7F_2$ transition is a typical electric dipole transition and strongly varies with the local symmetry of Eu^{3+} ions, while the $^5D_0 \rightarrow {}^7F_1$ transition corresponds to a parity-allowed magnetic dipole transition, which is practically independent of the host material. Among these transitions, $^5D_0 \rightarrow {}^7F_1$ transition shows the strongest emission, suggesting the chemical environment around Eu^{3+} ions is in high symmetry [36, 37]. According to the Judd–Ofelt theory, the magnetic dipole transition is permitted; however, the electric dipole transition is allowed only when the europium ion occupies a site without an inversion center, and the intensity is significantly affected by the symmetry in local environments around Eu^{3+} ions [38]. On the contrary, when the Eu^{3+} ion occupies a site with an inversion center, then $^5D_0 \rightarrow {}^7F_1$ should be relatively strong, while the $^5D_0 \rightarrow {}^7F_2$ transition should be relatively weak. According to the above results, more Eu^{3+} ions have occupied the inversion sites in CeF_3: Eu^{3+} nanoparticles. As a result, the strong orange–red luminescence was observed in the emission spectra which indicated that the effective energy transfer took place between the Ce^{3+} and the central Eu^{3+} ions. In addition, the emission spectrum of these mesoporous materials contains not only the emission of Eu^{3+} ion but also a broad emission band in the blue spectral region peaking around 460 nm. Compared with the typical emissions of the central Eu^{3+}, the broad emission band mainly originated from the emission of the host SBA-15. Furthermore, upon illumination of the materials by three different methods with a UV lamp, the resulting CeF_3: Eu^{3+}/SBA-15/SS shows an orange–red light and much stronger luminescence, which is in agreement with emission spectra. As a result, the luminescence intensities of the $^5D_0 \rightarrow {}^7F_1$ transition for the three kinds of mesoporous materials were all compared. It is interesting that the major peak positions in the emission spectra are identical to these three samples, while the emission intensity of the materials using three methods is different. The relative intensity of CeF_3: Eu^{3+}/SBA-15/SS mesoporous material is stronger than that of CeF_3: Eu^{3+}/SBA-15/SI and CeF_3: Eu^{3+}/SBA-15/IS. In addition, the $^5D_0 \rightarrow {}^7F_1$ transition can be used as a reference to compare luminescent intensities of different Eu^{3+}-based materials due to its magnetic dipole nature. The relative luminescent intensities of the $^5D_0 \rightarrow {}^7F_1$ transition (I_{01}) and the $^5D_0 \rightarrow {}^7F_1/{}^5D_0 \rightarrow {}^7F_2$ intensity ratios (orange/red ratio) for all materials are listed in Table 2.

Luminescence Decay Times (τ) and Emission Quantum Efficiency (η)

The typical decay curve of all the CeF_3:Eu^{3+} functionalized mesoporous materials were measured at room temperature using a selective excitation wavelength of 395 nm, which can be assigned to the $f \rightarrow f$ transition of Eu^{3+}, and all the decay curves can be described as a single exponential ($\mathrm{Ln}(S(t)/S_0) = -k_1 t = -t/\tau$), indicating that all Eu^{3+} ions occupy the same average coordination

Table 2 Photoluminescent data of all mesoporous materials

	CeF_3: Eu^{3+}	CeF_3: Eu^{3+}/SBA-15/SI	CeF_3: Eu^{3+}/SBA-15/SS	CeF_3: Eu^{3+}/SBA-15/IS
v_{01} (cm^{-1})	17,006	17,006	17,006	17,006
v_{02} (cm^{-1})	16,260	16,260	16,260	16,556
v_{03} (cm^{-1})	15,432	15,432	15,432	15,432
v_{04} (cm^{-1})	14,472	14,285	14,306	14,306
I_{01}	942.9	227.5	454.1	159.5
I_{02}	336.2	85.9	159.8	99.2
I_{01}/I_{02}	2.80	2.65	2.84	1.61
τ (ms)	0.887	0.598	1.224	0.360
$1/\tau$ (ms^{-1})	1.127	1.672	0.817	2.778
A_r	204	177	186	128
A_{nr}	923	1,495	631	2,650
η (%)	18.1	10.6	22.8	4.6

environment. The lifetime data were given in Table 2. Furthermore, we selectively determine the emission quantum efficiencies of the $^5D_0$ europium ion-excited state for Eu^{3+} hybrids on the basis of the emission spectra and lifetimes of the $^5D_0$ emitting level. According to the emission spectrum and the lifetime of the Eu^{3+} first excited level (τ, $^5D_0$), the emission quantum efficiency (η) of the $^5D_0$ Eu^{3+} excited state can be determined. Assuming that only nonradiative and radiative processes are essentially involved in the depopulation of the $^5D_0$ state, η can be defined by radiative transition rate (A_r) and nonradiative transition rate (A_{nr}) [39], A_r can also be obtained by summing over the radiative rates A_{0J} for each $^5D_0 \rightarrow {}^7F_J$ ($J = 0$–4) transitions of Eu^{3+}. The branching ratio for the $^5D_0 \rightarrow {}^7F_{5,\ 6}$ transitions can be neglected as they are not detected experimentally, whose influence can be ignored in the depopulation of the $^5D_0$ excited state. Since $^5D_0 \rightarrow {}^7F_1$ belongs to the isolated magnetic dipole transition, it is practically independent of the chemical environments around the Eu^{3+} ion, and thus can be considered as an internal reference for the whole spectrum, the experimental coefficients of spontaneous emission, A_{0J} can be calculated according to the Einstein's coefficient of spontaneous emission between the $^5D_0$ and $^7F_1$ energy levels (A_{01}) and integrated intensities of $^5D_0 \rightarrow {}^7F_J$ transitions ($J = 1$–4) [40]. In addition, A_{01} as a value of 14.65 s^{-1} in vacuum, when an average index of refraction n equal to 1.506 was considered, the value of A_{01} can be determined to be 50 s^{-1} approximately ($A_{01} = n^3 A_{01\ (vac)}$) [41]. On the basis of reference [42–44], the value of $A_{01} \approx 50\ s^{-1}$ and the lifetime (τ), radiative (A_r), and nonradiative (A_{nr}) transition rates are related through the following equation:

$$A_{tot} = 1/\tau = A_r + A_{nr}$$

On the basis of the above discussion, the quantum efficiencies of the four kinds of europium mesoporous hybrid materials can be determined, as shown in Table. 2. As can be clearly seen from Table 2, the quantum efficiencies of CeF_3: Eu^{3+}/SBA-15/SS ($\eta = 22.77\%$) is higher than that of CeF_3: Eu^{3+}/SBA-15/SI and CeF_3: Eu^{3+}/SBA-15/IS, which is in agreement with the intensity of the emission spectra. Furthermore, CeF_3: Eu^{3+}/SBA-15/IS ($\eta = 4.61\%$) exhibits much lower emission quantum efficiency than CeF_3: Eu^{3+}/SBA-15/SS ($\eta = 22.77\%$), which indicates that the deposition of CeF_3: Eu^{3+} onto the mesoporous framework of SBA-15 using in situ method has greatly influenced the luminescence of Eu^{3+} ion in CeF_3: Eu^{3+}. Further, we selectively determined the energy transfer efficiency for the three kinds of mesoporous materials. For these functionalized mesoporous SBA-15 by CeF_3: Eu^{3+} mesoporous materials, S-I, I-S, and S-S systems, CeF_3 plays two roles: both the host and the energy donor for Eu^{3+} (energy acceptor).The energy transfer efficiency from CeF_3 to Eu^{3+} of CeF_3: Eu^{3+}/SBA-15/SS (76%) is higher than that of CeF_3: Eu^{3+}/SBA-15/SI (55%) and CeF_3: Eu^{3+}/SBA-15/IS (38%). This is due to the different reaction condition, the contribution of energy transfer efficiency of CeF_3 decreases in the total luminescence quantum efficiency of Eu^{3+}.

Ultraviolet–Visible Diffuse Reflection Absorption Spectra

The ultraviolet–visible diffuse reflection absorption spectroscopy of CeF_3: Eu^{3+}/SBA-15/SI, CeF_3: Eu^{3+}/SBA-15/IS, and CeF_3: Eu^{3+}/SBA-15/SS are given in Fig. 7. It is observed that the bands of all the mesoporous materials are located at about 250–375 nm, which partially overlaps with the luminescent excitation spectra (wide bands at 290–350 nm in Fig. 6a). It is worth noting that CeF_3: Eu^{3+}/SBA-15/SS obviously shows three well-resolved absorption peaks at 246, 229, and 259 nm for the Ce^{3+}, while the other two materials CeF_3: Eu^{3+}/SBA-15/IS and CeF_3: Eu^{3+}/SBA-15/SS contain not only the typical emissions of Ce^{3+} ion but also a broad region peaking around 350 nm, originated from the absorption of the matrix.

Conclusion

In summary, we have designed novel luminescent mesoporous materials by the deposition of a CeF_3: Eu^{3+} phosphor layer onto the channel surface of mesoporous SBA-15 using three different methods: reaction in situ (I-S), solution impregnation (S-I), and solid phase grinding synthesis (S-S), respectively. The corresponding composite materials were denoted as CeF_3: Eu^{3+}/SBA-15/IS, CeF_3: Eu^{3+}/SBA-15/SI, and CeF_3: Eu^{3+}/SBA-15/SS. The synthesis of this

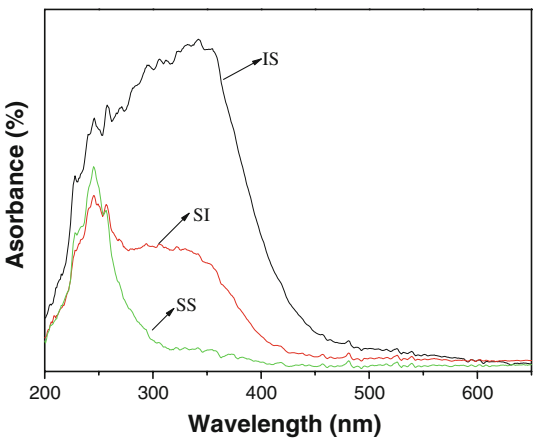

Fig. 7 The ultraviolet–visible diffuse reflection absorption spectra of CeF_3: Eu^{3+}/SBA-15/SI, CeF_3: Eu^{3+}/SBA-15/IS, and CeF_3: Eu^{3+}/SBA-15/SS

system provides a convenient approach of tailoring the surface properties of mesoporous silicates by nanophosphor functionalization, and the resulting materials all retain the ordered mesoporous structures. Further investigation into the luminescence properties of CeF_3: Eu^{3+}/SBA-15 mesoporous materials shows that the characteristic luminescence of the corresponding Eu^{3+} through the energy transfers from the Ce^{3+} to the central Eu^{3+} ions. As a result, more Eu^{3+} ions have occupied the inversion sites in CeF_3: Eu^{3+} nanoparticles, resulting in that magnetic dipole transition $^5D_0 \rightarrow {}^7F_1$ (588 nm) are the dominant bands for the materials. Meantime, the CeF_3: Eu^{3+}/SBA-15/SS exhibits the higher luminescence intensity than the other two materials. So it can be concluded that the obtained samples using different synthesis methods show different luminescence properties, which can be related to the guest–host interactions between the guest molecule and the silica matrix.

Acknowledgments This work was supported by the National Natural Science Foundation of China (20971100) and Program for New Century Excellent Talents in University (NCET-08-0398).

References

1. K. Kömpe, H. Borchert, J. Storz, A. Lobo, S. Adam, T. Möller, M. Haase, Angew. Chem. Int. Ed. **42**, 5513 (2003)
2. J.W. Stouwdam, G.A. Hebbink, J. Huskens, F.C.J.M. van Veggel, Chem. Mater. **15**, 4604 (2003)
3. S. Heer, O. Lehmann, M. Haase, H. Gudel, Angew. Chem. Int. Ed. **42**, 3179 (2003)
4. F. Meiser, C. Cortez, F. Caruso, Angew. Chem. Int. Ed. **43**, 5954 (2004)
5. W. Bu, Z. Hua, H. Chen, J. Shi, J. Phys. Chem. B **109**, 14461 (2005)
6. Q. Li, L. Gao, D.S. Yan, Chem. Mater. **11**, 533 (1999)
7. Y.W. Zhang, X. Sun, R. Si, L.P. You, C.H. Yan, J. Am. Chem. Soc. **127**, 3260 (2005)
8. M.M. Lezhnina, T. Justel, H. Katker, D.U. Wiechert, U.H. Kynast, Adv. Funct. Mater. **16**, 935 (2006)
9. Z.L. Wang, Z.W. Quan, P.Y. Jia, C.K. Lin, Y. Luo, F. Chen, J. Fang, W. Zhou, C.J. O'Connor, J. Lin, Chem. Mater. **18**, 2030 (2006)
10. R.J. Yan, Y.D. Li, Adv. Funct. Mater. **15**, 763 (2005)
11. K. Shimamura, E.G. V'llora, S. Nakakita, M. Nikl, N. Ichinose, J. Cryst. Growth **264**, 208 (2004)
12. G.S. Yi, G.M. Chow, J. Mater. Chem. **15**, 4460 (2005)
13. X. Wang, J. Zhuang, Q. Peng, Y.D. Li, Inorg. Chem. **45**, 6661 (2006)
14. M.E. Davis, Nature **417**, 813 (2002)
15. A. Stein, Adv. Mater. **15**, 763 (2003)
16. Q.H. Xu, L.S. Li, B. Li, R.R. Xu, Micropor. Mesopor. Mater. **38**, 351 (2005)
17. A. Fernandes, J. Dexpert-Ghys, A. Gleizes, A. Galarneau, D. Brunel, Micropor. Mesopor. Mater. **83**, 35 (2005)
18. M.S. Zhang, W. Yin, Q. Su, H.J. Zhang, Mater. Lett. **57**, 940 (2002)
19. Q.H. Xu, L.S. Li, X.S. Liu, R.R. Xu, Chem. Mater. **14**, 549 (2002)
20. D.Y. Zhao, J.P. Feng, Q.S. Huo, N. Melosh, G.H. Fredrickson, B.F. Chmelka, G.D. Stucky, Science **79**, 348 (1998)
21. Y. Han, D. Li, L. Zhao, F.S. Xiao, Angew. Chem. Int. Ed. **42**, 3633 (2003)
22. Y. Han, F.S. Xiao, S. Wu, J. Phys. Chem. B **105**, 7963 (2001)
23. Y. Liu, W. Zhang, T.J. Pinnavaia, Angew. Chem. Int. Ed. **40**, 1255 (2001)
24. B. Munoz, A. Ramila, J. Pe′rez-Pariente, I. Dıaz, M. Vallet-Regı, Chem. Mater. **15**, 500 (2003)
25. C. Barbe, J. Bartlett, L. Kong, K. Finnie, H.Q. Lin, M. Larkin, S. Calleja, A. Bush, G. Calleja, Adv. Mater. **16**, 1949 (2004)
26. Y. Li, B. Yan, H. Yang, J. Phys. Chem. C **112**, 3959 (2005)
27. P.P. Yang, S.S. Huang, D.Y. Kong, J. Lin, H.G. Fu, Inorg. Chem. **46**, 3203 (2004)
28. D.L. Shi, J. Lian, W. Wang, G.K. Liu, P. He, Z.Y. Dong, L.M. Wang, R.C. Ewing, Adv. Mater. **18**, 189 (2006)
29. Y.S. Lin, S.H. Wu, Y. Hung, Y.H. Chou, C. Chang, M.L. Lin, C.P. Tsai, C.Y. Mou, Chem. Mater. **18**, 5170 (2006)
30. M.V. Landau, S.P. Parkey, M. Herskowitz, O. Regev, S. Pevzner, T. Sen, Z. Luz, Micropor. Mesopor. Mater. **33**, 149 (1999)
31. M. Yu, J. Lin, J. Fang, Chem. Mater. **17**, 1783 (2005)
32. L. Zhu, Q. Li, X.D. Liu, J.Y. Li, Y.F. Zhang, J. Meng, X.Q. Cao, J. Phys. Chem. C **111**, 5898 (2007)
33. D.G. Everett, Pure Appl. Chem. **31**, 577 (1972)
34. K.S.W. Sing, D.H. Everett, R.A. Haul, L. Moscow, R.A. Pierotti, J. Rouquerol, T. Siemieniewska, Pure Appl. Chem. **57**, 603 (1985)
35. M.H. Lim, A. Stein, Chem. Mater. **11**, 3285 (1999)
36. P. Miranda Jr, J. Zukerman-Schpector, P.C. Isolani, G. Vicentini, L.B. Zinner, J. Alloys Compd. **344**, 141 (2002)
37. X.M. Guo, L.S. Fu, H.J. Zhang, L.D. Carlos, C.Y. Peng, J.F. Guo, J.B. Yu, R.P. Deng, L.N. Sun, New J. Chem. **29**, 1351 (2005)
38. J. Dexpert-Ghys, R. Mauricot, M.D. Faucher, J. Lumin. **27**, 203 (1996)
39. P.C.R. Soares-Santos, H.I.S. Nogueira, V. Félix, M.G.B. Drew, R.A.S. Ferreira, L.D. Carlos, T. Trindade, Chem. Mater. **15**, 100 (2003)
40. E.S. Teotonio, J.G.P. Espínola, H.F. Brito, O.L. Malta, S.F. Oliveria, D.L.A. de Foria, C.M.S. Izumi, Polyhedron **21**, 1837 (2002)
41. M.H.V. Werts, R.T.F. Jukes, J.W. Verhoeven, Phys. Chem. Chem. Phys. **4**, 1542 (2004)
42. J.C. Boyer, F. Vetrone, J.A. Capobianco, A. Speghini, M. Bettinelli, J. Phys. Chem. B **108**, 20137 (2004)
43. S.T. Frey, M.L. Gong, W.D. Horrocks Jr, Inorg. Chem. **33**, 3229 (1994)
44. O.L. Malta, H.J. Batista, L.D. Carlos, Chem. Phys. **282**, 21 (2002)